Prospects for photon-pair generation using silicon microring resonators with two photon absorption and free carrier absorption

CHAOXUAN MA,[1] AND SHAYAN MOOKHERJEA[1,*]

[1] *University of California, San Diego, Department of Electrical and Computer Engineering, La Jolla, California 92093-0407, USA*
[*] *smookherjea@ucsd.edu*

Abstract: Silicon microring resonators are being recently used for high-brightness and efficient photon-pair generation at telecommunications wavelengths. Here, based on detailed theoretical and numerical modeling, we study the impact on pair generation of increasing the optical pump power, which generally causes nonlinear impairments such as free-carrier and two-photon absorption in silicon micro-resonators. Contrary to expectation, the pair generation properties of such devices may seem to be preserved at increasing pump powers, although not better than at a moderate pump power. These results suggest that silicon microrings can be used for pair generation over a wide range of pump powers, which may benefit applications in remotely-pumped architectures, where the pump level might not be known a priori.

1. Introduction

Photon pair generation in silicon microring resonators using the process of spontaneous four wave mixing (SFWM) is being recognized as an attractive platform for quantum optics and quantum communications using information encoded onto single photons [1–3]. From a technology viewpoint, these devices are compatible with the classical integrated photonics technology fabricated on large-area silicon wafers, which is being rapidly adopted in industry for its low cost, high performance and scalability. It has been known from the early days of silicon photonics that, at higher levels of pump powers, especially in the continuous-wave (CW) regime, silicon photonic devices suffer from not only thermally-induced spectral shifts (which can be compensated by feedback-stabilization to the laser) but also nonlinear impairments such as nonlinear two-photon absorption and free-carrier absorption, which cannot be eliminated, even with carrier sweepout schemes [4,5].

The process of SFWM is itself a nonlinear optical process involving an optical pump. Photon-pair generation can be observed at relatively small levels of pump powers (less than one milliwatt) in waveguides, but the optical intensity can be significantly enhanced in micro-resonator devices, thus bringing additional physical phenomena into consideration. In silicon waveguides, the effective nonlinear coefficient

$$\gamma = \frac{2\pi n_2}{\lambda_p A_{eff}} \tag{1}$$

which is a function of the nonlinear refractive index n_2, pump wavelength λ_p, and optical effective mode area A_{eff}, is typically in the range of 100 – 200 W.m^{-1} [6–8]. A simple waveguide, however, has a broad emission spectral span (typically from one to tens of nanometers) [9,10] which lacks brightness, coherence and purity, unless followed by a narrow bandpass filter. The resulting rate of photon generation is then reduced, and furthermore, the spectrum of the bi-photon state is modified by the properties of the filters. Narrowband filters typically have a bandwidth ranging from 0.1 to several nanometers, with the disadvantages of high insertion loss, cost and limited scalability [11,12].

In contrast to waveguides, integrated micro-resonators incorporate the nonlinear segment into a relatively high-Q micro-cavity, thus greatly increasing the nonlinear interaction length between the pump, signal and idler frequencies without increasing the device footprint on the chip [13,14]. A typical value of the unloaded Q factor in experimentally demonstrated silicon microrings can be close to one million. The pump and photon-pair modes match selected cavity modes which are phase-matched, while also satisfying energy conservation. Stringent dispersion engineering is not required in typical silicon waveguides around the wavelength of 1550 nm since the group index of refraction is approximately constant, and, in practice, the pump, signal and idler wavelengths are taken to be fairly close to each other.

In micro-resonators, the circulating pump intensity is significantly enhanced through resonance, which results in a stronger and more efficient nonlinear process. The cavity itself serves as a narrowband filter, which, if properly designed, can more easily achieve a smaller bandwidth than external filters, since no "margin" needs to be reserved to keep separate structures aligned through experimental temperature fluctuations. This integrated approach can result in a substantial increase in the overall brightness of pair generation, but the locally-increased intensity of the pump beam, as seen by the silicon material, leads to a number of different physical phenomena brought into play, which result in easily-visible characteristics of the (high pump-power induced) nonlinear regime [15].

In the following sections, we will model the SFWM process with a continuous-wave pump beam, which models a number of recent experimental reports [16–20]. Waveguide SFWM or spontaneous parametric down-conversion (SPDC) experiments typically shape the pump beam into ultrashort pulses, in order to match the very wide phase-matching bandwidth. For SFWM in silicon microresonators, pulse widths less than about 50 ps are rarely required, and thus, the CW (or quasi-CW) regime is a useful analytical and numerical approximation to help elucidate the complicated dynamics in the high-power regime.

2. Photon-pair generation and nonlinear impairments

The pair generation rate (R) in a silicon microring resonator can be calculated by using the following equation [14]:

$$R = \Delta\nu[\gamma P^{\mathrm{res}} L_{\mathrm{eff}}^{\mathrm{res}}]^2 \,\mathrm{sinc}^2(\beta_2 \Delta\omega^2 \frac{L^{\mathrm{res}}}{2} + \gamma P^{\mathrm{res}} L_{\mathrm{eff}}^{\mathrm{res}}) \tag{2}$$

where $\Delta\nu$ is the full width half maximum (FWHM) of the ring resonance, γ is the effective waveguide nonlinearity, β_2 is the group velocity dispersion (GVD) coefficient of the waveguide which constitutes the microring resonator at the pump wavelength, $\Delta\omega$ is the pump-signal (idler) angular frequency separation, P^{res}, L^{res}, and $L_{\mathrm{eff}}^{\mathrm{res}}$ are the resonantly-enhanced power, length and loss-scaled effective interaction length parameters, whose expressions are obtained by conceptually unfolding the resonator into a waveguide, with appropriately defined enhancement factors:

$$P^{\mathrm{res}}(\lambda) = P_0 \times \frac{1-r^2}{(1-ra)^2} \times \frac{(\frac{\lambda_{\mathrm{p}}}{2Q})^2}{(\lambda-\lambda_{\mathrm{p}})^2 + \frac{\lambda_{\mathrm{p}}}{2Q}} \tag{3}$$

$$L^{\mathrm{res}} = L \times \frac{F}{\pi} \tag{4}$$

$$L_{\text{eff}}^{\text{res}} = \frac{1-\exp(-\alpha L)}{\alpha} \times \frac{F}{\pi} \tag{5}$$

P_0 is the input pump power in the access waveguide, α is the waveguide propagation loss of the pump, F and Q are the finesse and quality factor (Q-factor) of the resonator. For a microring resonator in the all-pass configuration (i.e., coupled to one waveguide, rather than two),

$$F = \frac{\pi\sqrt{ra}}{1-ra} \tag{6}$$

$$Q = \frac{\pi n_g L\sqrt{ra}}{\lambda_{\text{res}}(1-ra)} \tag{7}$$

where r is the (amplitude) self-coupling coefficient, $a = \exp(-\alpha L/2)$ is the amplitude round-trip transmission of the cavity, n_g is the group index of refraction of the waveguide.

In practice, however, Eq. (2) does not include all the factors that affects photon pair generation in a resonator cavity. Since these resonators [21–23] are usually designed to have a high loaded Q-factor (~1×10^4 - 1×10^5) in order to enhance the pump power intensity and thus source efficiency, a series of linear or nonlinear processes can be induced by the high intensity in the cavity. Fig. 1(a) shows a classical measurement of a silicon microresonator (microdisk) spectra at different input power levels. The power was recorded when a tunable laser was swept from short to long wavelengths. The lineshape and position of the resonance was clearly changed with the input power level. The asymmetric lineshape under the swept-wavelength scanning indicated thermal bistability. The behavior of the silicon microresonator under high input pump power is a combined consequence of two-photon absorption (TPA), free carrier absorption (FCA), free carrier dispersion (FCD) and thermo-optic effects [24], which will be modeled in the following sections.

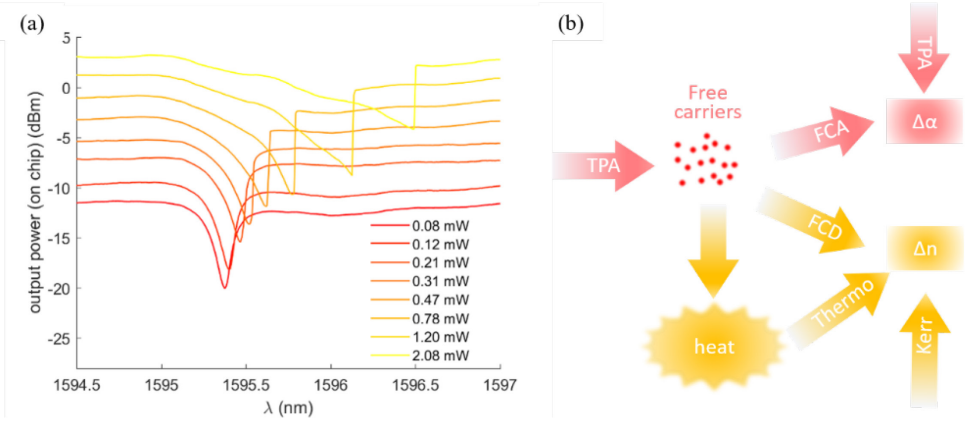

Fig. 1. (a) Experimentally measured silicon microdisc resonator spectra, measured using a swept-wavelength tunable laser, at different input power levels. As the input power scales up, the resonance red shifts and extinction degrades. (b) Some of the physical processes impacting pair generation in a silicon photonic device when the pump power is high, which involves two-photon absorption (TPA), free carrier absorption (FCA), free carrier dispersion (FCD) and thermo-optic effect.

Two Photon Absorption

The refractive index difference between silicon (the waveguide core) and silicon dioxide (cladding) provides for a strong optical mode confinement in silicon photonic waveguides. The local intensity of light is further increased by the feedback effect in cavity-based devices, when

the pump wavelength matches the cavity resonance. For photon pair generation, this enhancement is a boon in terms of the generation efficiency at low pump power, but has the (obvious) consequence of inducing TPA at high pump power level.

TPA occurs when the sum of two input photons' energy is higher than silicon's bandgap (1.12 eV) and the local optical intensity is high, thus resulting in a high probability (per second) of optically-induced carrier excitation events across the bandgap, leading to absorption of the pump light, and typically, generation of heat. Photons that are absorbed also generally create a free carrier, as indicated schematically in Fig. 1(b). The strength of the TPA interaction is described by a coefficient $\beta_{\mathrm{TPA}} = [3\pi / (c\grave{o}_0 \lambda / n_0^2)]\,\mathrm{Im}\{\chi^{(3)}\}$ [25], which depends on the silicon crystal orientation and the wavelength. The loss induced by TPA can be calculated as

$$\alpha_{\mathrm{TPA}} = \beta_{\mathrm{TPA}} I \tag{8}$$

where I is the optical intensity. In a high-confinement waveguide, the average TPA loss across the spatial variation of the mode intensity profile can be expressed as

$$\bar{\alpha}_{\mathrm{TPA}} = \frac{\int_{Si} \beta_{\mathrm{TPA}} I^2(\mathbf{r})\mathrm{d}A}{\int_{\infty} I(\mathbf{r})\mathrm{d}A} \approx \frac{\beta_{\mathrm{TPA}} P^{\mathrm{res}}}{A_{\mathrm{eff}}} \tag{9}$$

For SFWM in silicon photonic devices, TPA manifests itself as a propagation loss in the pump power, especially when reverse-biased carrier sweepout is no longer able to extract the photo-generated electronic carriers [26], and a significant reduction in the interaction length (i.e., number of round trips that the pump light makes in the resonator). This is, intuitively, not of benefit for SFWM, and thus, it is reasonable to suppose that SFWM in silicon micro-resonators should exclusively be performed at low optical pump powers, lest there be a steep roll-off in performance at higher pump powers [27]. However, the results shown here suggest that additional considerations should be taken into account.

Free Carrier Absorption and Free Carrier Dispersion

Free carriers are generated by TPA and cause subsequent effects including free carrier absorption (FCA) and free carrier dispersion (FCD). The free carriers generated by TPA can be described by a Drude-like model [28,29]. After the carriers are generated, their spatial density profile is redistributed by diffusion. To simplify the model in our analysis here, we neglect the longitudinal diffusion of carriers along the pump propagation direction, and we only consider lateral diffusion in a waveguide cross section. The time-dependent carrier density in a silicon waveguide can be expressed as [30]

$$\frac{dN}{dt} = \frac{\beta_{\mathrm{TPA}} I^2}{2h\nu} + D' \frac{\partial^2 N}{\partial^2 x} - \frac{N}{\tau_{\mathrm{c}}} \tag{10}$$

where N is the carrier density, $h\nu$ is the photon energy, D' is the effective diffusion constant of the free carriers and τ_{c} is the effective carrier recombination time. For CW pumping, $dN/dt = 0$ and, further setting $\partial^2 N / \partial^2 x = 0$, the steady-state carrier density can be written as [31]

$$N = \frac{\beta_{\mathrm{TPA}} I^2 \tau_0}{2h\nu} \tag{11}$$

These free carriers result in both a waveguide loss and a plasma dispersion effect, which is related to the induced carrier density by [28]

$$\alpha_{\mathrm{FC}} = \frac{e^3 \lambda^2}{4\pi^2 c^2 \grave{o}_0 n} \left(\frac{\Delta N_{\mathrm{e}}}{m_{ce}^2 \mu_e} + \frac{\Delta N_h}{m_{ch}^2 \mu_h} \right) = \sigma N(z,t) \tag{12}$$

$$\Delta n_{\mathrm{FC}} = -\frac{e^2\lambda^2}{8\pi^2 c^2 \varepsilon_0 n}\left(\frac{\Delta N_e}{m_{\mathrm{ce}}} + \frac{\Delta N_h}{m_{\mathrm{ch}}}\right) \approx -8.2\times10^{-22}\lambda^2 N(z,t) \tag{13}$$

where $\sigma \approx 1.45\times10^{-17}[\mathrm{cm}^2]\left(\lambda(\mathrm{nm})/1550\right)^2$ is the free carrier absorption cross-section area. The average FCA induced loss is then calculated as

$$\bar{\alpha}_{\mathrm{FC}} = \frac{\int_{Si}\sigma N(z,t) I(\mathbf{r})\mathrm{d}A}{\int_{\infty} I(\mathbf{r})\mathrm{d}A} = \frac{\sigma\beta_{\mathrm{TPA}}\tau_0}{2h\nu}\frac{(P^{\mathrm{res}})^2}{A'_{\mathrm{eff}}A_{\mathrm{eff}}} \tag{14}$$

where A'_{eff} is an effective area defined as

$$A'_{\mathrm{eff}} = \frac{\int_{\infty} I(\mathbf{r})\mathrm{d}A \int_{\infty} I^2(\mathbf{r})\mathrm{d}A}{\int_{\mathrm{Si}} I^3(\mathbf{r})\mathrm{d}A} \tag{15}$$

Thermo-Optic Effect

The loss mechanisms including TPA (α_{TPA}), FCA (α_{FC}) and material absorption (α_{m}) also result in a temperature increase in silicon waveguides (and, obviously, resonators), which in turn causes an index change of the optical mode via the thermo-optic effect:

$$\Delta n = \frac{\mathrm{d}n}{\mathrm{d}T}\Delta T \tag{16}$$

where dn/dT for silicon is quite high (~ 2×10^{-4} K^{-1}) compared to other materials. The time-dependent temperature change induced by TPA can be expressed as

$$\frac{\mathrm{d}\Delta T}{\mathrm{d}t} = \frac{(\alpha_{\mathrm{TPA}} + \alpha_{\mathrm{FC}} + \alpha_{\mathrm{m}})I}{\rho_{\mathrm{Si}}C_{\mathrm{Si}}} - \frac{\Delta T}{\tau_{\mathrm{th}}} \tag{17}$$

where ρ_{Si} is the mass density of silicon, C_{Si} is the specific heat capacity of silicon and τ_{th} is the heat dissipation time. For complex, multi-layer devices, computational models are being investigated which can solve for the steady-state temperature distribution efficiently [32]. Here, under CW pumping when $\mathrm{d}\Delta T / \mathrm{d}t = 0$, the temperature shift of the device is calculated using

$$\Delta T(z,t) = \frac{\tau_{\mathrm{th}}(\alpha_{\mathrm{TPA}} + \alpha_{\mathrm{FCA}} + \alpha_{\mathrm{m}})}{\rho_{\mathrm{Si}}C_{\mathrm{Si}}} I(z,t) = \frac{\tau_{\mathrm{th}}(\beta_{\mathrm{TPA}} I(z,t) + \alpha_{\mathrm{FC}} + \alpha_{\mathrm{m}})}{\rho_{\mathrm{Si}}C_{\mathrm{Si}}} I(z,t) \tag{18}$$

A Numerical Model for SFWM in Microrings

The optical characteristics of the resonator cavity are driven by the input power P_0, which causes a change in the resonantly enhanced quantities: P^{res}, $L_{\mathrm{eff}}^{\mathrm{res}}$ and L^{res}. A full spatio-temporal numerical solution is too complex and computationally cumbersome to be useful for obtaining physical insights. Our key simplifying assumptions are: (1) The wavelength of the pump is always positioned at the resonance (in practice, this is achieved by monitoring for the resonance, e.g., using a photodiode); (2) The absolute change in the waveguide refractive index, which is induced by the steady state contribution of the combination of the Kerr nonlinearity, the FCD and the thermo-optic effect, can be neglected since it can be compensated for, by an active control circuit using thermal tuning of the microring [33,34]; (3) Due to (2), the change of waveguide-cavity coupling strength is negligible; (4) For a comparison between sources with different bandwidths, the photon pairs will be filtered by a 1-nm (approximately 100 GHz) bandwidth optical filter (assumed to have no insertion loss) which will ensure the spectral purity of the photons. (5) Photons are transmitted in loss-free channels and detected by single photon

detectors with a detection efficiency of 95%, comparable with what can be achieved using superconducting single photon detectors.

The total loss in the cavity is a combination of material absorption (α_m), TPA (α_{TPA}) and FCA (α_{FC}):

$$\alpha_{total} = -(\alpha_{TPA} + \alpha_{FC} + \alpha_m) \tag{19}$$

According to Eq. (3), we have

$$P_0 = \frac{P^{res}(1-ra)^2}{1-r^2} \tag{20}$$

Note that the round-trip amplitude transmission a is a function of P^{res}, which makes the right side of the equation a (monotonic) function of P^{res}. Eq. (20) can be numerically solved and the cavity loss can also be determined. The photon PGR can then be calculated using Eq. (2), which quantifies the intra-cavity generation rate. The extracted (i.e., output) pair generation rate also includes the extraction efficiency, i.e., the fraction of the photon pairs which are coupled out of the microring into the bus waveguide. We approximate the on-resonance extraction efficiency as [22]

$$\eta_p = \frac{1 \pm \sqrt{(T_c)}}{2} \tag{21}$$

where T_c is the transmissivity at resonance, and the plus and minus signs correspond to over-coupled and under-coupled conditions. The probability of coupling both photons in a pair out of cavity is η_p^2. Note that the number of extracted photon pairs is less than the extracted idler or signal photons, i.e., photon pairs are broken due to the non-unity extraction efficiency. The photons remaining out of broken pairs may later contribute to the accidental coincidences if they propagate all the way to the SPDs.

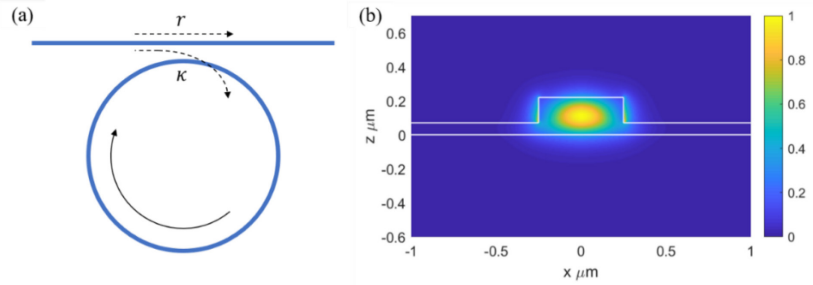

Fig. 2. (a) Schematic drawing of an optical ring resonator, where coefficients r and κ are the electric-field amplitude transmittance and cross-coupling coefficients, respectively. (b) Optical mode profile (magnitude of the transverse electrical field) for the transverse-electric (TE) mode in a typical single-mode silicon rib waveguide. The waveguide cross section is 220 nm thick and 500 nm wide, with a slab height of 70 nm.

We simulated a silicon photonic microring whose cavity consists of a rib waveguide with a radius of 10 μm. The SOI platform has a 220 nm-thick silicon layer sandwiched between buried and cladding oxide. The rib waveguide is 500 nm wide with a slab height of 70 nm. This is a typical design of single-mode silicon waveguide which, unlike a fully-etched waveguide, can be heated efficiently by contacting a section of the (high-resistivity) slab at some distance safely off to the side of the optical mode with metal vias and traces, and driving an electrical current. The optical mode was calculated using the finite-difference eigenmode solver in Lumerical Mode Solutions™; a representative mode is shown in Fig. 2(b). The characteristics of the optical mode and other relevant parameters are listed in **Table 1**.

Table 1 Values of relevant parameters used in calculations

Parameters	Value
α_m	0.7 dB/cm
A_{eff}	0.171 μm^2
A'_{eff}	0.124 μm^2
GVD	-1223 ps/nm·km
n_{eff}	2.53
n_g	4.0
n_2	6×10^{-18} m^2/W
β_{TPA}	0.8 cm/GW [6]
τ_c	0.8 ns
τ_{th}	1 μs
dn/dT	1.84×10^{-4} /K
C_{Si}	705 J/(kg·K)
ρ_{Si}	2.3×10^{-3} kg/m^3
η_{det}	0.95
D	100 Hz
Laser sidemode-suppression ratio	60 dB/nm
$\Delta\tau$	10 ps

Based on the numerical solutions, the change in the cavity is shown in Fig. 3. Here, we simulated a microring resonator with a coupling strength $|\kappa|^2$ of 0.01. Initially, the waveguide was assumed to have a linear propagation loss of 0.7 dB/cm, which typically includes the loss contributions from material absorption, waveguide bending and scattering due to the roughness of waveguide walls. The Q-factor of the ring was then calculated to be 9.2×10^4. As the input power scales up, TPA was observed to become more significant, as expected, and both TPA and TPA-induced FCA increase. For input power higher than about 0.37 mW in our simulations, FCA was observed to take over as the dominant loss mechanism. This results in a reduced cavity loaded Q-factor, which drops quickly once FCA dominates the cavity loss, as shown in Fig. 3(b).

In the same figure, we have shown how the intracavity resonant power scales with the input power. While the intracavity power scales linearly in a TPA-free cavity as shown in blue dashed line (the resonant enhancement factor is constant), the benefit of increasing input power becomes smaller in a nonlinear cavity for the high-power regime, as a consequence of the degraded loaded Q-factor.

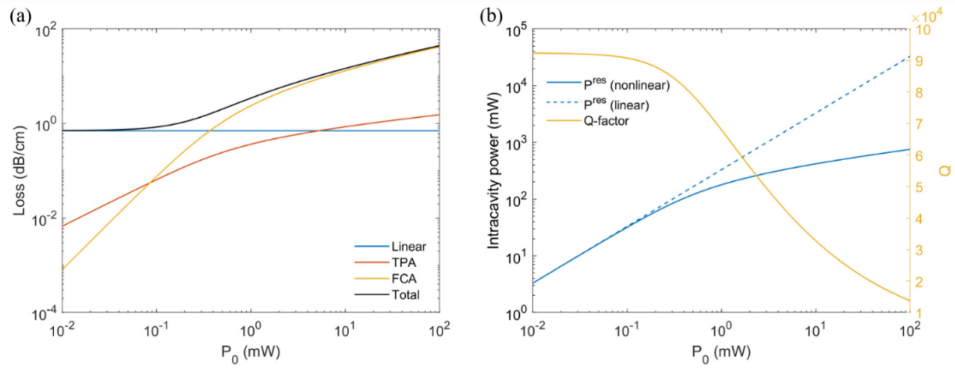

Fig. 3. Change inside the microring cavity consisting of waveguide shown in Fig. 2(b), assuming a constant (amplitude) coupling strength in the coupling region of 0.01. (a) Loss composition as a function of input power. To start with, there is linear absorption losses such as material absorption loss and scattering loss. As the input power increases, TPA produces free carriers which induce FCA. FCA becomes dominant at high input power levels. (b) Intracavity resonant power and Q-factor of the cavity as a function of input power. The blue dash line is the resonant power in an ideal linear cavity. The blue solid line is the power inside a nonlinear cavity. As the input power increases, Q-factor of the cavity degrades, and the resonant enhancement effect is not as strong. The rate gap between a nonlinear and linear cavity widens.

3. Pair generation characteristics in the nonlinear regime

PGR reflects the trend shown in Fig. 4. In a TPA-free cavity, PGR as a function of input power exhibits the same trend as PGR as a function of $|\kappa|^2$ [14], i.e., the increasing intracavity power increases the self-phase modulation (SPM) term in the phase matching 'sinc^2' term in Eq. (2), hence leading to the multiple dips in the high power regime. In practice, the optical power would have to very carefully adjusted and stabilized, in order to not result in significant swings in the PGR. (Long integration times in an experiment will typically average out these fluctuations, but result in a low average rate, overall.)

In a nonlinear cavity, TPA and TPA-induced FCA prevent the intracavity power to scale with the input power as fast as in a linear cavity, thus the change in the SPM term has been slowed down significantly. In fact, with these simulated values of the key parameters, the first dip of the phase-matching term does not appear within the reasonable pump power regions (< 1W). In this respect, these loss mechanisms have actually stabilized the cavity for pair generation, which would otherwise have been highly sensitive to the input power level and exact value of the waveguide-cavity coupling strength $|\kappa|^2$. Of course, this benefit comes with some penalty in PGR, relative to what could have been achieved if nonlinear loss was absent. Moreover, the extraction efficiency is also decreased when the coupling condition goes from over-coupling to under-coupling, which can impact the heralding efficiency. Nevertheless, since nonlinear loss cannot be avoided in silicon, the stabilization is expected to be of considerable benefit practically. Furthermore, the predicted PGR, despite the penalty, is quite high: a maximum PGR (extracted) of 55 MHz may be obtained at an input power of 1.7 mW for this ring design ($|\kappa|^2 = 0.01$), which would be comparable to many state-of-the-art SPDC devices, in a much more compact footprint, at lower pump powers, and using only simple materials such as silicon and oxide, which have no requirement for poling.

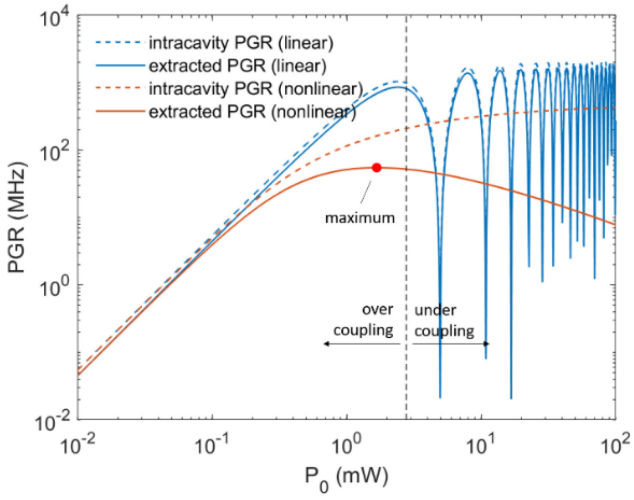

Fig. 4. PGR inside the microring cavity consisting of waveguide shown in Fig. 2(b), when $|\kappa|^2 = 0.01$. TPA and its-induced FCA prevent the intracavity power from scaling with the input power as fast as it is in a linear cavity, Thus the increase in the SPM term in phase matching term also slows down significantly, which prevents the sinc^2 term to appear in the high power region. As the input power increases, the cavity changes from over-coupled to under-coupled, thus the extraction efficiency of the photon pairs are also compromised. The overall extracted PGR reaches a maximum of 55 MHz at the input power of 1.7 mW.

4. Discussion

A more comprehensive sweep of all $|\kappa|^2$ and P_0 combinations, as shown in Fig. 5(b) and (d) obtained a maximum PGR (extracted) of 75 MHz with a CAR of 577 at $|\kappa|^2 = 0.089$ and $P_0 = 31.6$ mW. Fig. 5(a) and (c) shows the otherwise PGR if the cavity is TPA-free. In the lower-right corner, that is, high Q-factor and high power region, PGR is ultra-sensitive to the input pump power and waveguide-cavity coupling ratio, which manifests itself in the dips that are too dense to see clearly. The TPA and its-induced FCA effects removes most of the dips in the reasonable pump power levels (<1 W), which significantly relaxes the requirements for fabrication and power level accuracy.

Another distinction from the two types of resonators is the mechanisms for reaching an optimum PGR when ramping up the input pump power: for an ideal TPA-free resonator, the local optimum PGR is caused by the phase matching "sinc^2" terms, while in a practical cavity, the PGR is limited by the cavity extraction efficiency. Although increasing the input pump power can, in theory, always increase the intracavity PGR, the extraction efficiency of the photon pairs degrades as the cavity loss scales up. Therefore, the extracted PGR cannot grow infinitely.

The CAR is mainly decided by the relative strength of true coincidences and accidentals, that is

$$\text{CAR} = \frac{C_{\text{cc}} - C_{\text{acc}}}{C_{\text{cc}}} \tag{22}$$

where C_{cc} and C_{acc} are the raw detected coincidences and accidental coincidences, which can be calculated as

$$C_{cc} = R_{\text{pair}}\eta_{\text{i}}\eta_{\text{s}} \tag{23}$$

$$C_{acc} = \Delta\tau[(R_{\text{i}} + R_{\text{n,i}})\eta_{\text{i}} + D_{\text{i}}][(R_s + R_{\text{n,s}})\eta_s + D_s] \tag{24}$$

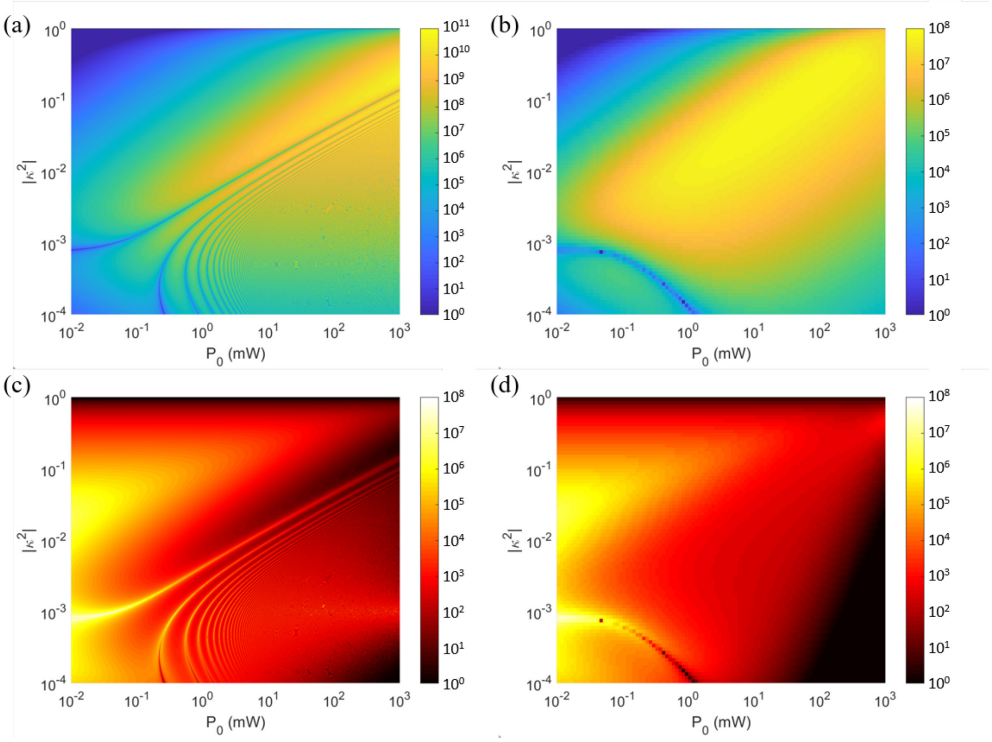

Fig. 5. Extracted PGR (a) (in Hz) and CAR (c) (in log scale) as a function of input power and $|\kappa|^2$ in a TPA-free cavity. The right lower corner contains very fine and dense ripples representing the fast oscillating phase matching term (sinc^2) induced by high intracavity power. Extracted PGR (b) and CAR (c) (in log scale) as a function of input power and $|\kappa|^2$ in a nonlinear cavity. All calculations are based on the microring cavity consisting of waveguide shown in Fig. 2(b).

where R_{pair} is the intra-cavity PGR, η_s (η_i) is the extraction efficiency of the signal (idler) photons, $R_{n,s}$ ($R_{n,i}$) and D_s (D_i) are the noise photon rate and detector dark count rate in the signal (idler) channel, and $\Delta\tau$ is the coincidence window for the measurement.

Note that, according to Eq. (23) and (24), the CAR can be increased by decreasing $\Delta\tau$, the time window over which coincidence counts are measured. Here, we used a uniform value of $\Delta\tau$ for all calculations so that the relative trends can be observed independently of the specific value. The value that was used, $\Delta\tau = 10$ ps, as stated in Table 3, is consistent with the low jitter values of modern superconducting nanowire single-photon detectors (which can be less than 5 ps full-width at half-maximum at 1550 nm wavelengths) [35], the timing resolution of time-correlated single-photon counting (TCSPC) instruments (typically, 1 ps), and the values of the resulting instrument response function (IRF), which can be less than 10 ps [36]. Higher values of $\Delta\tau$ because of experimental limitations will result in decreased CAR measurements.

The ASE noise and residual pump scales linearly with the input pump power, while the rate of noise photons from broken pairs generally increases quadratically with the pump power in the lower power region (and slowly saturates and then declines as the power increases further), so does the true coincidence rates. However, given Eq. (24), the relationship between the input pump power and accidentals coincidences should be further "squared" which allows the accidentals to increase faster than true coincidences.

In Fig. 5(d), the two most bright regions where CAR is high are those where the pump powers are lowest. The first of these two regions is located where the process of photon pair generation is the most efficient. Interestingly, the second region sits in the valley of the phase matching "sinc-squared" term, which suggests that the broken-pair-related accidentals are suppressed to a greater extent by the dip of that term, compared to the effect of the sinc-squared

term on the true coincidences. On the contrary, the other end of the P_0 - $|\kappa|^2$ dip line becomes the local minimum of the CAR map in Fig. 5(d) (i.e., indicative of worse performance), where accidentals quickly scale up with the input pump power.

Fig. 6(a) shows the choice of $|\kappa|^2$ that maximize extracted PGR for each input pump power level. Fig. 6(b) shows the photon pair characteristics, CAR and FWHM, for each combination of $|\kappa|^2$ and P_0. With TPA, the extracted PGR reaches maximum at $|\kappa|^2 = 0.089$ and $P_0 = 31.6$ mW. The relative fast drop at the high power regime is due to the 1-nm filtering after pair generation, which ensures the bandwidth of the photon pairs is not excessively wide. Within a range of pump powers from 0.5 mW ($|\kappa|^2 = 0.0075$) to 630 mW ($|\kappa|^2 = 0.316$), the extracted PGR is always higher than one-half of the maximum, and the value of CAR is relatively stable (1245 for 0.5mW, 616 for 630 mW). The only quantity that appears to change drastically is the FWHM of the generated photon pairs, which scales from 16 pm all the way up to 1 nm (restricted, in our set of calculation assumptions, by the bandwidth of the filter).

In most cases, one would prefer to operate in the low pump region (in this case, 0.5 mW) with a higher CAR and narrower FWHM of photon pairs without sacrificing much PGR. On one hand, the ring has a much higher photon pair generation *efficiency* in the lower power region, although not necessarily the highest overall generation *rate*. From a practical perspective, the linear regime is also more stable and amenable to feedback-stabilization. In experimental measurements, a two-photon (Franson type) interference measurement on the signal and idler photons, with the inclusion of 1 nm passband filters on both output channels, resulted in CAR of about 500 and fringe visibilities of 98%, using pump powers between 0.25 mW and 0.4 mW, depending on the wavelength [37]. The degree of entanglement at the higher pump powers has not been experimentally studied, being limited at present by the fiber-to-waveguide coupling losses. The upper limit on the visibility due to multiphoton events is approximately given by $V_{max} = 1-\alpha$ where α is the pair generation number per detection gate [38,39]. Assuming a maximum rate of 75 MHz (which is higher than what today's practical detector can accommodate), α = (75 MHz).(10 ps) = 0.08%, so $V_{max} \sim 100\%$. A wider coincidence detection window e.g., assuming that $\Delta\tau = 256$ ps, for example, results in $V_{max} \sim$ 98.1%. However, typical detection rates are only a few MHz, with most of the difference between generation rate and detection rate attributed to the channel loss, and thus, multi-photon events are not expected to contribute to a limit on the visibility in the regime studied here, even at the larger detection windows. A practical limit may, instead, be due to accidental coincidences or dispersion between the signal and idler photons.

A larger waveguide-resonator coupling coefficient strength is required to match a high pump power (e.g. $|\kappa|^2 \sim 0.316$ for a pump power of 630 mW). There may be some technical difficulties to realize this level of coupling: The ring is usually too small to realize a long-enough coupling region. Although one can reduce the gap between waveguide and the ring cavity to reduce the required coupling length, it usually cannot be made smaller than about 150 nm, based on typical fabrication tolerances in a foundry silicon photonics process. Different in-plane coupler designs [40], or vertical inter-layer couplers [41,42] may be interesting designs for further study and generation of actual device layouts.

One factor not accounted for in detail in these calculations is the noise contribution of the nonlinear two-photon absorption [9]. Specifically, noise photons can be generated through a four-wave mixing process seeded by loss-induced noise, through coupling to a photon reservoir, whose occupancy statistics can be modeled as thermal. However, the effect is not likely to be large for range of parameters considered here. For a microring resonator with FSR = 10 nm, and diameter 10 μm (approximately), at the highest intra-cavity pump powers (P_{res}) considered in Fig. 3, at which $Q = 1.5\text{x}10^4$ and Finesse $F \approx 31\pi$, the factor $|\gamma P_{res} L_{res}| \sim 200$ $(\text{W.m})^{-1}$.(0.4 W).(1 mm) ≈ 0.08, well below the threshold value (0.2) considered to be indicative of significance. Furthermore, since the noise process has a delayed temporal response compared with the near-instantaneous SFWM process, it may be possible to apply mode-selective filtering that can reject most of the noise photons and improve two-photon visibility [43].

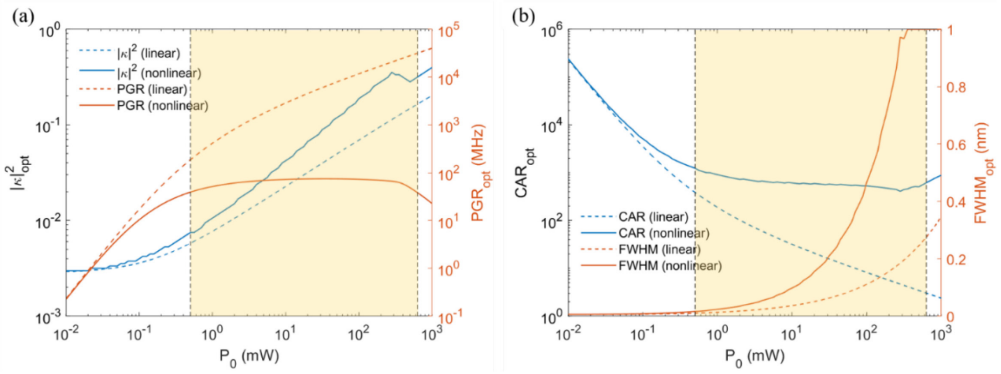

Fig. 6. Photon pair characteristics for the combinations of $|\kappa|^2$ and P_0 to maximize PGR. (a) Optimum $|\kappa|^2$ as a function of input pump power to maximize the PGR (extracted). The dash lines are reference $|\kappa|^2$ (dash blue) and PGR (dash orange) for a TPA-free resonator. The solid lines are reference $|\kappa|^2$ (solid blue) and PGR (solid orange) for a nonlinear cavity where TPA can occur. (b) CAR and the resonance's FWHM as a function of the input pump power for the maximized PGR (extracted). The dash lines are reference CAR (dash blue) and FWHM (dash orange) for a TPA-free cavity. The solid lines are reference CAR (solid blue) and FWHM (solid orange) for a nonlinear cavity where TPA can occur. The shaded area (light yellow) is where the extracted PGR is within half of its maximum for a TPA-enabled resonator.

Waveguide Engineering

The design of waveguide affects the photon pair generation process in the following ways: (1) the dispersion of the waveguide in the phase matching "sinc-squared" term determines the sensitivity of the device performance to design parameters, fabrication errors and input pump power; (2) The waveguide propagation loss, together with the waveguide-cavity coupling strength, decides the Q-factor of the cavity, hence the pair generation efficiency; (3) The size of the optical mode effective area is inversely proportional to the strength of the waveguide nonlinearity.

Given that the dispersion, loss and mode confinement of the waveguide are usually inter-dependent, it is not straightforward to identify which waveguide cross-section best optimizes the PGR or photon quality. To discuss a representative example, we search here for a waveguide cross-section which maximizes PGR. Some of the results are shown in Fig. 7, which shows the calculated PGR as a function of the input pump power (P_0) and waveguide-cavity coupling strength ($|\kappa|^2$). (Simulations at other thicknesses give qualitatively similar observations.) The dashed line in each subfigure shows the optimum $|\kappa|^2$ which maximizes the PGR for each value of the input pump power. The white dots enclose the half-maximum region where the PGR is more than half of the maximum. The GVD is shown in the upper-left corner of each subfigure.

While there are more dips [from the phase matching term in Eq. (2)] for the high-Q, low power regions in a waveguide with higher dispersion, this might not be a concern if the coupling strength can be designed within the half-maximum region, which is defined by the intersection of the black dash line and the white-dotted boundary, at a safe distance from the "oscillating" region of the parameter space. Once the coupling strength is higher than a threshold value (the starting value of the black dash line), one may not fall into the dips whatever the pump power level. Experimentally, one may wish to choose the lowest pump power point on the border of the half-maximum region which will optimize the generation efficiency of the photon pairs. These simulations also suggest that, as a general rule, the pair generation microring should always be designed to operate in the over-coupling regime in order to optimize the pair generation efficiency. Compared to the under-coupled or critically-coupled cases, the over-coupled microring has a higher extraction efficiency (of the photons generated internally in the resonator to the output bus waveguide), which not only improves the CAR but also the heralding efficiency of the photon pairs.

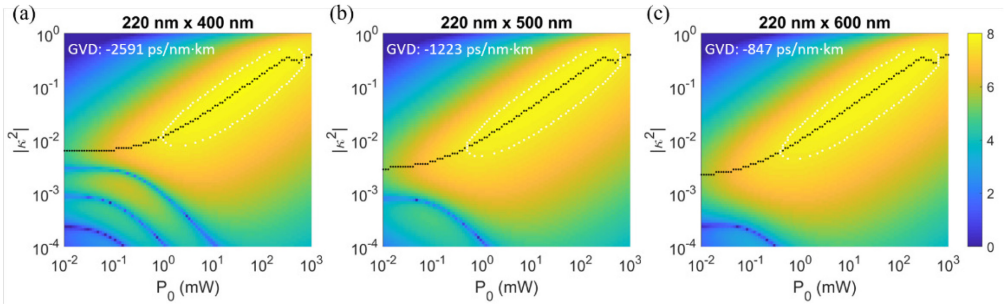

Fig. 7. PGR (units: number of pairs per second, or Hz) as a function of input pump power P_0 and waveguide-cavity coupling strength $|\kappa|^2$ for different waveguide cross sections, labeled at the top of each sub-panel by the waveguide height x waveguide width. (The slab height is 70 nm.) The group velocity dispersion is shown in the upper-left corner of each subfigure. The dashed line in each subfigure is optimum $|\kappa|^2$ to maximize PGR for each input pump power. The colorbar indicates the exponent of the PGR, i.e., values of 0 to 8 represent PGR values of 1 Hz to 1E8 Hz, respectively.

We scanned the cross section of a silicon rib waveguide to obtain its maximum PGR. Typically, silicon-on-insulator (SOI) layer stack used in silicon photonics has a silicon device layer thickness in the range of 200 nm to 400 nm. We have also varied the width of the rib from 300 nm to 800 nm. The height of the slab is kept at 70 nm. It is shown in Fig. 8(a) that a smaller cross section is more favorable to obtain a higher pair generation capacity. The maximum PGR is obtained in the smallest waveguide cross section (200 nm thick, 300 nm wide) with a calculated value of 120 million pairs per second capable of being generated at an input power of about 90 mW, while achieving a CAR of 343. While this number does not consider experimental imperfections and challenges e.g., the tuning capability of the resonance stabilization system, and extra propagation loss, it gives an upper bound of the pair generation capability of a silicon photonic microring.

At this time, most of the experimental demonstrations have focused on sub-milliwatt pumping of silicon photonic microrings [1,14,21,23,44,45]. In the low pump power region, TPA and the induced FCA effects are not as significant and the power generation efficiency as well as CAR can be much higher, as shown in Fig. 6(b). We simulated the maximum PGR that can be obtained by 1 mW input pump power for each cross section, with the results shown in Fig. 8(c). Generally, increasing the waveguide cross-section area increases the pair generation capability. A maximum PGR (extracted) of 58 million pairs per second can be obtained at 1 mW input pump power, using a waveguide cross section of 340 nm-thick and 650 nm-wide (a slab height of 70 nm).

The differences between Fig. 8(a) and Fig. 8(c) are more clearly shown in Fig. 8(d), where the maximum PGR as a function of input pump power is calculated for 220 nm-thick waveguide cross section. While waveguides with a larger cross-section can have higher pair generation efficiencies, PGR saturates earlier due to stronger TPA effects, which limits the pair generation capacity. It is also noted that after increasing the width to 500 nm for a 220 nm thick rib waveguide, the benefit of increasing the width further is minimal. Thus, the waveguide cross section can be designed using a relatively small cross section, which can help in maintaining single-mode operation without sacrificing the pair generation capacity.

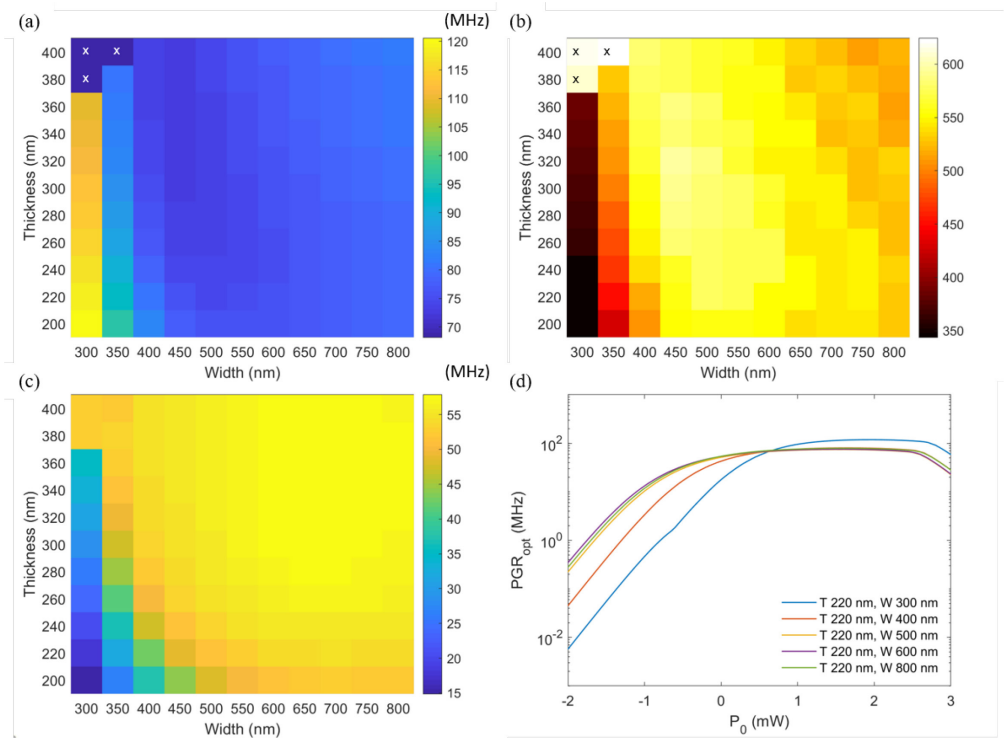

Fig. 8. (a)-(b) Maximum PGR (a) and its corresponding CAR (b) as a function of waveguide cross section geometry. The cells denoted by crosses correspond to waveguide cross sections whose fundamental mode is TM mode. (c) Maximum PGR for input pump power of 1 mW as a function of waveguide cross section geometry. (d) Maximum PGR as a function of each input pump power level for 220 nm-thick cross sections.

5. Conclusions

A set of simulations have been performed for the photon pair-generation process, based on SFWM in high-Q silicon microring resonators. Such devices are known to exhibit nonlinear behavior in the high optical pump power regime, when the optical power level in the feeder waveguide typically exceeds a few milliwatts. While the thermal effects can possibly be compensated for by feedback and tuning, the nonlinear loss effects can be quite severe. Our simulation results show that, in this nonlinear regime, the pair generation capability (in terms of the rate of photon pairs that can be extracted from the device) is surprisingly tolerant to the design of the coupler between the waveguide and resonator, which happens to be the main contribution of fabrication errors in these devices. Certain other parameters, e.g., the spectral full-width at half-maximum of the two-photon state, may, however, increase continuously with pump power. Since this is also important for indistinguishability and purity of the quantum state, the coupling strength need still be carefully selected. Taken together, these results suggest that the notorious sensitivity to the exact design parameters of a high-Q microring resonator may, at least in the case of silicon, be fortuitously stabilized, rather than destablized, by the predominant nonlinear effects of two-photon absorption and free-carrier absorption, which may benefit the process of photon-pair generation at fairly high rates, exceeding several tens of millions of photon pairs per second.

Funding

NSF (CNS-1525090, EFMA-1640968); IBM PhD Fellowship Program.

Disclosures

The authors declare no conflicts of interest.

References

1. L. Caspani, C. Xiong, B. J. Eggleton, D. Bajoni, M. Liscidini, M. Galli, R. Morandotti, and D. J. Moss, "Integrated sources of photon quantum states based on nonlinear optics," Light Sci Appl **6**, e17100–e17100 (2017).
2. C. M. Gentry, J. M. Shainline, M. T. Wade, M. J. Stevens, S. D. Dyer, X. Zeng, F. Pavanello, T. Gerrits, S. W. Nam, R. P. Mirin, and M. A. Popović, "Quantum-correlated photon pairs generated in a commercial 45 nm complementary metal-oxide semiconductor microelectronic chip," Optica **2**, 1065–1071 (2015).
3. L.-T. Feng, G.-C. Guo, and X.-F. Ren, "Progress on Integrated Quantum Photonic Sources with Silicon," Adv. Quantum Technol. **3**, 1900058 (2020).
4. A. Liu, H. Rong, R. Jones, O. Cohen, D. Hak, and M. Paniccia, "Optical Amplification and Lasing by Stimulated Raman Scattering in Silicon Waveguides," J. Lightwave Technol. **24**, 1440 (2006).
5. K. K. Tsia, S. Fathpour, and B. Jalali, "Energy harvesting in silicon wavelength converters," Opt. Express **14**, 12327–12333 (2006).
6. M. Dinu, F. Quochi, and H. Garcia, "Third-order nonlinearities in silicon at telecom wavelengths," Appl. Phys. Lett. **82**, 2954–2956 (2003).
7. R. L. Espinola, J. I. Dadap, R. M. Osgood, S. J. McNab, and Y. A. Vlasov, "C-band wavelength conversion in silicon photonic wire waveguides," Opt. Express **13**, 4341–4349 (2005).
8. K. Yamada, H. Fukuda, T. Tsuchizawa, T. Watanabe, T. Shoji, and S. Itabashi, "All-optical efficient wavelength conversion using silicon photonic wire waveguide," IEEE Photon. Technol. Lett. **18**, 1046–1048 (2006).
9. Q. Lin and G. P. Agrawal, "Silicon waveguides for creating quantum-correlated photon pairs," Opt. Lett. **31**, 3140–3142 (2006).
10. J. E. Sharping, K. F. Lee, M. A. Foster, A. C. Turner, B. S. Schmidt, M. Lipson, A. L. Gaeta, and P. Kumar, "Generation of correlated photons in nanoscale silicon waveguides," Opt. Express **14**, 12388–12393 (2006).
11. J. R. Ong, R. Kumar, and S. Mookherjea, "Ultra-High-Contrast and Tunable-Bandwidth Filter Using Cascaded High-Order Silicon Microring Filters," IEEE Photon. Technol. Lett. **25**, 1543–1546 (2013).
12. M. Piekarek, D. Bonneau, S. Miki, T. Yamashita, M. Fujiwara, M. Sasaki, H. Terai, M. G. Tanner, C. M. Natarajan, R. H. Hadfield, J. L. O'Brien, and M. G. Thompson, "High-extinction ratio integrated photonic filters for silicon quantum photonics," Opt. Lett. **42**, 815 (2017).
13. W. C. Jiang, X. Lu, J. Zhang, O. Painter, and Q. Lin, "Silicon-chip source of bright photon pairs," Opt. Express **23**, 20884–20904 (2015).
14. M. Savanier, R. Kumar, and S. Mookherjea, "Photon pair generation from compact silicon microring resonators using microwatt-level pump powers," Opt. Express **24**, 3313–3328 (2016).
15. Y. Guo, W. Zhang, N. Lv, Q. Zhou, Y. Huang, and J. Peng, "The impact of nonlinear losses in the silicon micro-ring cavities on CW pumping correlated photon pair generation," Opt. Express **22**, 2620–2631 (2014).
16. X. Shi, K. Guo, J. B. Christensen, M. A. U. Castaneda, X. Liu, H. Ou, and K. Rottwitt, "Multichannel Photon-Pair Generation with Strong and Uniform Spectral Correlation in a Silicon Microring Resonator," Phys. Rev. Appl. **12**, 034053 (2019).
17. R. R. Kumar, X. Wu, and H. K. Tsang, "Compact high-extinction tunable CROW filters for integrated quantum photonic circuits," Opt. Lett. **45**, 1289–1292 (2020).
18. C. Wu, Y. Liu, X. Gu, X. Yu, Y. Kong, Y. Wang, X. Qiang, J. Wu, Z. Zhu, X. Yang, and P. Xu, "Bright photon-pair source based on a silicon dual-Mach-Zehnder microring," Sci. China Phys. Mech. Astron. **63**, 220362 (2019).
19. J. A. Steidle, C. C. Tison, M. L. Fanto, M. L. Fanto, S. F. Preble, and P. M. Alsing, "Highly Directional Silicon Microring Photon Pair Source," in *Conference on Lasers and Electro-Optics* (Optical Society of America, 2019) paper FTh1D.4.
20. F. A. Sabattoli, H. E. Dirani, F. Garrisi, S. Sam, C. Petit-Etienne, J. M. Hartmann, E. Pargon, C. Monat, M. Liscidini, C. Sciancalepore, M. Galli, and D. Bajoni, "A Source of Heralded Single Photon Using High Quality Factor Silicon Ring Resonators," in *2019 21st International Conference on Transparent Optical Networks (ICTON)* (IEEE, 2019), paper Th.C2.4.
21. C. Ma, X. Wang, V. Anant, A. D. Beyer, M. D. Shaw, and S. Mookherjea, "Silicon photonic entangled photon-pair and heralded single photon generation with CAR > 12,000 and g^(2)(0) < 0006," Opt. Express **25**, 32995 (2017).
22. X. Lu, S. Rogers, T. Gerrits, W. C. Jiang, S. W. Nam, and Q. Lin, "Heralding single photons from a high-Q silicon microdisk," Optica **3**, 1331–1338 (2016).
23. J. W. Silverstone, R. Santagati, D. Bonneau, M. J. Strain, M. Sorel, J. L. O'Brien, and M. G. Thompson, "Qubit entanglement between ring-resonator photon-pair sources on a silicon chip," Nat Commun **6**, 1–7 (2015).
24. V. R. Almeida, C. A. Barrios, R. R. Panepucci, and M. Lipson, "All-optical control of light on a silicon chip," Nature **431**, 1081–1084 (2004).
25. X. Sang, E.-K. Tien, and O. Boyraz, "Applications of two-photon absorption in silicon," J. Optoelectron. Adv. Mat. **11**, 15–25 (2008).

26. J. R. Ong, R. Kumar, R. Aguinaldo, and S. Mookherjea, "Efficient CW Four-Wave Mixing in Silicon-on-Insulator Micro-Rings With Active Carrier Removal," IEEE Photon. Technol. Lett. **25**, 1699–1702 (2013).
27. C. A. Husko, A. S. Clark, M. J. Collins, A. D. Rossi, S. Combrié, G. Lehoucq, I. Rey, T. F. Krauss, C. Xiong, and B. J. Eggleton, "Cross-absorption as a limit to heralded silicon photon pair sources," in *Nonlinear Optics and Its Applications VIII; and Quantum Optics III* (International Society for Optics and Photonics, 2014), Vol. 9136, paper 91361O.
28. R. Soref and B. Bennett, "Electrooptical effects in silicon," IEEE J. Quantum Electron. **23**, 123–129 (1987).
29. A. J. Sabbah and D. M. Riffe, "Femtosecond pump-probe reflectivity study of silicon carrier dynamics," Phys. Rev. B **66**, 165217 (2002).
30. Y. Liu and H. K. Tsang, "Time dependent density of free carriers generated by two photon absorption in silicon waveguides," Appl. Phys. Lett. **90**, 211105 (2007).
31. G. T. Reed, *Silicon Photonics: The State of the Art* (John Wiley & Sons, 2008).
32. X. Wang and S. Mookherjea, "Fast circuit modeling of heat transfer in photonic integrated circuits," in *2017 Conference on Lasers and Electro-Optics (CLEO)*, JW2A (2017).
33. M. Savanier, R. Kumar, and S. Mookherjea, "Optimizing photon-pair generation electronically using a p-i-n diode incorporated in a silicon microring resonator," Appl. Phys. Lett. **107**, 131101 (2015).
34. K. Guo, L. Yang, X. Shi, X. Liu, Y. Cao, J. Zhang, X. Wang, J. Yang, H. Ou, and Y. Zhao, "Nonclassical Optical Bistability and Resonance-Locked Regime of Photon-Pair Sources Using Silicon Microring Resonator," Phys. Rev. Applied **11**, 034007 (2019).
35. B. Korzh, Q.-Y. Zhao, J. P. Allmaras, S. Frasca, T. M. Autry, E. A. Bersin, A. D. Beyer, R. M. Briggs, B. Bumble, M. Colangelo, G. M. Crouch, A. E. Dane, T. Gerrits, A. E. Lita, F. Marsili, G. Moody, C. Peña, E. Ramirez, J. D. Rezac, N. Sinclair, M. J. Stevens, A. E. Velasco, V. B. Verma, E. E. Wollman, S. Xie, D. Zhu, P. D. Hale, M. Spiropulu, K. L. Silverman, R. P. Mirin, S. W. Nam, A. G. Kozorezov, M. D. Shaw, and K. K. Berggren, "Demonstration of sub-3 ps temporal resolution with a superconducting nanowire single-photon detector," Nat. Photonics **14**, 250–255 (2020).
36. X. Wang, A. E. Dane, K. K. Berggren, M. D. Shaw, S. Mookherjea, B. A. Korzh, P. O. Weigel, D. J. Nemchick, B. J. Drouin, W. Becker, Q.-Y. Zhao, D. Zhu, and M. Colangelo, "Oscilloscopic Capture of Greater-Than-100 GHz, Ultra-Low Power Optical Waveforms Enabled by Integrated Electrooptic Devices," J. Lightwave Technol. **38**, 166–173 (2020).
37. C. Ma and S. Mookherjea, "Simultaneous dual-band entangled photon pair generation using a silicon photonic microring resonator," Quantum Sci. Technol. **3**, 034001 (2018).
38. I. Marcikic, H. de Riedmatten, W. Tittel, V. Scarani, H. Zbinden, and N. Gisin, "Time-bin entangled qubits for quantum communication created by femtosecond pulses," Phys. Rev. A **66**, 062308 (2002).
39. T. Zhong, "High-dimensional entanglement-based quantum key distribution," PhD Thesis (Department of Electrical Engineering and Computer Science, Massachusetts Institute of Technology, 2013).
40. N. Eid, R. Boeck, H. Jayatilleka, L. Chrostowski, W. Shi, and N. A. F. Jaeger, "FSR-free silicon-on-insulator microring resonator based filter with bent contra-directional couplers," Opt. Express **24**, 29009–29021 (2016).
41. P. P. Absil, J. V. Hryniewicz, B. E. Little, F. G. Johnson, K. J. Ritter, and P.-T. Ho, "Vertically coupled microring resonators using polymer wafer bonding," IEEE Photon. Technol. Lett. **13**, 49–51 (2001).
42. D. V. Tishinin, P. D. Dapkus, A. E. Bond, I. Kim, C. K. Lin, and J. O'Brien, "Vertical resonant couplers with precise coupling efficiency control fabricated by wafer bonding," IEEE Photon. Technol. Lett. **11**, 1003–1005 (1999).
43. Y.-P. Huang and P. Kumar, "Distilling quantum entanglement via mode-matched filtering," Phys. Rev. A **84**, 032315 (2011).
44. S. Clemmen, K. P. Huy, W. Bogaerts, R. G. Baets, P. Emplit, and S. Massar, "Continuous wave photon pair generation in silicon-on-insulator waveguides and ring resonators," Opt. Express **17**, 16558–16570 (2009).
45. N. C. Harris, D. Grassani, A. Simbula, M. Pant, M. Galli, T. Baehr-Jones, M. Hochberg, D. Englund, D. Bajoni, and C. Galland, "Integrated Source of Spectrally Filtered Correlated Photons for Large-Scale Quantum Photonic Systems," Phys. Rev. X **4**, 041047 (2014).